UC Irvine
UC Irvine Previously Published Works

Title

Manipulating electronic phase separation in strongly correlated oxides with an ordered array of antidots

Permalink

https://escholarship.org/uc/item/1b65r5jd

Journal

Proceedings of the National Academy of Sciences of the United States of America, 112(31)

ISSN

Authors

Zhang, Kai
Du, Kai
Liu, Hao
et al.

Publication Date

2015-08-04

DOI

Copyright Information

Peer reviewed

Manipulating electronic phase separation in strongly correlated oxides with an ordered array of antidots

Kai Zhang[a,b], Kai Du[a,b], Hao Liu[a,b], X.-G. Zhang[c], Fanli Lan[a,b], Hanxuan Lin[a,b], Wengang Wei[a,b], Yinyan Zhu[a,b], Yunfang Kou[a,b], Jian Shao[a,b], Jiebin Niu[a,b], Wenbin Wang[a,b], Ruqian Wu[a,b], Lifeng Yin[a,b,d,1], E. W. Plummer[e,1], and Jian Shen[a,b,d,1]

[a]Department of Physics, Fudan University, Shanghai 200433, China; [b]State Key Laboratory of Surface Physics, Fudan University, Shanghai 200433, China; [c]Quantum Theory Project, Department of Physics, University of Florida, Gainesville, FL 32611; [d]Collaborative Innovation Center of Advanced Microstructures, Nanjing 210093, China; and [e]Department of Physics and Astronomy, Louisiana State University, Baton Rouge, LA 70808

The interesting transport and magnetic properties in manganites depend sensitively on the nucleation and growth of electronic phase-separated domains. By fabricating antidot arrays in La$_{0.325}$Pr$_{0.3}$Ca$_{0.375}$MnO$_3$ (LPCMO) epitaxial thin films, we create ordered arrays of micrometer-sized ferromagnetic metallic (FMM) rings in the LPCMO films that lead to dramatically increased metal–insulator transition temperatures and reduced resistances. The FMM rings emerge from the edges of the antidots where the lattice symmetry is broken. Based on our Monte Carlo simulation, these FMM rings assist the nucleation and growth of FMM phase domains increasing the metal–insulator transition with decreasing temperature or increasing magnetic field. This study points to a way in which electronic phase separation in manganites can be artificially controlled without changing chemical composition or applying external field.

manganites | metal–insulator transition | electronic phase separation | antidot | magnetization

Electronic phase separation (EPS) is a striking phenomenon that commonly occurs in strongly correlated materials such as high-Tc oxides and colossal magnetoresistive (CMR) manganites (1, 2). Because EPS originates from strong coupling between spin, charge, orbital, and lattice, studies of EPS may reveal the fundamentals of strong electronic interactions in complex oxides (3, 4). Moreover, physical properties of complex oxides often depend sensitively on the details of EPS domains, including their size, density, and growth kinetics upon changing physical parameters. Therefore, a great effort has been devoted to study the EPS phenomena and engineer the domains in complex oxides (5, 6).

With the help of real-space imaging methods, the size of EPS domains of oxide films has been shown to range from ~10 nm to a few hundred nanometers, depending on the material (7, 8). The spatial distribution of the EPS domains is often random, and their shape can be tuned by external strain (9, 10) or the symmetry of substrates (11). Recently, it has been shown that the nucleation and growth of EPS domains in manganites are controllable by applying local external fields (magnetic or electric) (12, 13). What has not been explored is the effect of ordered arrays of artificially structured domains on EPS.

In this work, we show that ordered arrays of EPS domains can be created with controllable size, shape, and density in La$_{0.325}$Pr$_{0.3}$Ca$_{0.375}$MnO$_3$ (LPCMO), a prototypical CMR material. Specifically, we fabricate patterned arrays of holes, often referred to as negative dots or "antidots," (14–16) in the epitaxial LPCMO thin films. Ferromagnetic metallic (FMM) rings were observed surrounding the edges of the antidots, which is consistent with the recent discovery of FMM edge state in manganite strips (17). The magnetic measurements indicate that the magnetization of these rings is ~16% higher than that of the film. With the increase of antidot density, the LPCMO thin films exhibit considerably higher metal–insulator transition (MIT) temperature and lower resistivity. We propose a model that includes the nucleation effect of the FMM rings to explain the observed transport phenomena.

LPCMO films with 60-nm thickness are grown epitaxially on (001)-oriented SrTiO$_3$ substrates by ultrahigh vacuum pulsed-laser deposition. During the growing process, the system pressure is set to 3×10^{-3} torr with flowing oxygen and 8% ozone; the substrate temperature is kept at 800 °C (18). The layer-by-layer growth is monitored by reflection high-energy electron diffraction. The film is postannealed ex situ in flowing oxygen at 900 °C for 3 h. The antidots are fabricated by UV optical lithography and KI:HCl:H$_2$O (1:1:1) wet etching (17). For consistency, six samples, including five samples with different densities of uniform circular antidot (radius 1.2 μm) arrays and one control sample with no antidot, are fabricated from one single 5-mm × 5-mm film. Au electrodes with Cr buffer layers are patterned by optical lithography and grown by sputtering and lift-off method. Their resistances are measured by the four-point probe method (19) in a physical property measurement system, as illustrated in Fig. 1A. The effective area for all transport measurements is 500 μm × 1,000 μm (uniformly and fully filled with antidots) and the distances between the centers of the nearest antidots from lowest density to highest density (labeled D1 to D5) are 20, 10, 5, 4.1, and 3.3 μm, respectively. As an example, an SEM image of the second highest density antidot sample (D4) is shown in Fig. 1B.

Fig. 2 A–D shows the temperature dependence of normalized resistance (with respect to the resistance at 300 K) (6, 20) of different samples measured at 0-, 1-, 2-, and 5-T magnetic fields, respectively. The effect of imperfect shape of antidots, which is temperature-independent, can be excluded by using the normalized resistance. At zero and small fields, the samples with higher density antidots show considerably higher MIT temperatures, especially in the cooling process (solid line in Fig. 2). For

Significance

Electronic phase separation (EPS) is one of the most intriguing properties in complex materials. Great efforts have been made to understand or manipulate EPS, but how these phases are created and grow during percolation, let alone artificial control/fabrication of these phases, is still mysterious. In this work, we use a conceptual approach, i.e., fabricating antidots in manganites, and use their ferromagnetic metallic edge states to control the nucleation and growth of EPS domains. Consequently, we are able to tune the physical properties of the system without using external fields or changing doping concentration.
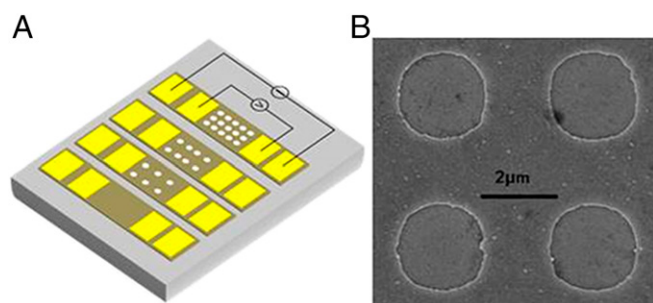
Fig. 1. (*A*) Schematic of the samples with different densities of antidot arrays. The golden square represents Au electrodes and the ammeter and voltmeter show the four-point probe method. (*B*) SEM image of the second highest density antidot sample (D4); the circles are the antidot holes fabricated by optical lithography and wet etching. The radius of the antidot is approximately 1.2 μm.

instance, at zero field (Fig. 2*A*), the MIT temperature of the highest density sample (D5) is about 40 K higher than that of the control sample. This enhancement is dramatic considering the fact that it is achieved with no change of doping concentration and no external field. In addition, samples with higher density antidots show smaller normalized resistance. In particular, the normalized resistance of the highest antidot density sample (D5) at the MIT temperature is about 60× smaller than that of the controlling film. By applying stronger magnetic field, the MIT temperatures of all samples increase and the differences between them become smaller. For example, the difference of MIT temperatures between the highest density sample (D5) and the controlling sample is less than 10 K at 5 T, as shown in Fig. 2*D*. The differences of the normalized resistance between samples also become smaller at large field, similar to the behavior of the MIT temperature.

Magnetic measurements indicate that the presence of antidots induces enhanced magnetization in the LPCMO films, which is consistent with the transport studies. Fig. 3 *A* and *B* shows the in-

plane and out-of-plane initial magnetization (dashed line) and hysteresis loops (solid line) at 10 K of a 60-nm-thick LPCMO film with and without the highest density (D5) antidots. With antidots, the saturation magnetization (M_s) of the film increases by 12% and 13% at low temperatures in the in-plane and out-of-plane directions, respectively. The steep rise of the initial magnetization at low field of the sample with antidots ends up with a plateau that is considerably higher than that of the film sample without antidots in both the in-plane and out-of-plane directions. Obviously, the antidots produce a larger portion of ferromagnetic phases and higher magnetization during the phase separation process (21, 22).

The antidot-induced dramatic increase of the MIT temperature, decrease of the normalized resistance, and increase of magnetization appear to correlate strongly with the preferred FMM phase around their edges. Fig. 4 shows the magnetic force microscopy (MFM) images of the second lowest density antidot sample (D2) acquired at 200, 140, 80, and 20 K under 5-T field cooling and the corresponding resistivity vs. temperature (R–T) cooling curve. Whereas submicrometer ferromagnetic domains can be seen in regions away from the antidots (8, 17), clear preference of ferromagnetic phase can be observed at the edges of the antidots. We note that the observed ferromagnetic domains by MFM should correspond to the FMM phase in the LPCMO system with the particular Pr and Ca doping chosen in this work (7). The preferred FMM edge phase becomes even more distinguishable when the sample is cooled to low temperature, which is in stark contrast compared with the MFM images acquired from LPCMO films with no antidots (Fig. S1). Whereas nearly the whole sample area becomes ferromagnetic at 20 K and 5 T, ferromagnetic phase with much stronger signal appears around the edge of the antidots, forming arrays of ferromagnetic rings in the film. As clearly seen from the MFM image at 20 K in Fig. 4, the magnetization signal decays with distance away from the edge of the antidots, which implies that the FMM rings serve as nuclei for the growth of ferromagnetic domains (for detailed analysis, see the *Supporting Information*, Fig. S2). It is important to note here that the 5-T perpendicular field is used to get a
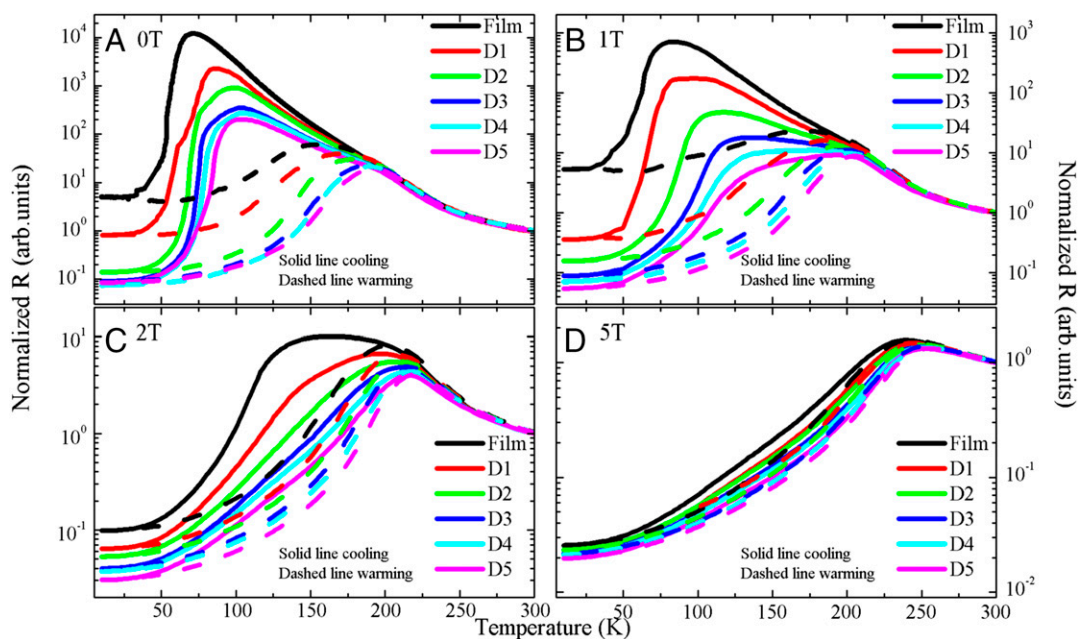
Fig. 2. Temperature dependence of normalized resistance for different density samples measured at (*A*) 0 T, (*B*) 1 T, (*C*) 2 T, and (*D*) 5 T. D1-5 represent the antidot samples with density from low to high. The solid lines show the cooling process and dashed lines show the warming process. In *A*, the samples with higher antidot density show higher MIT temperature and lower resistance. With increasing magnetic field in *B*–*D*, the differences become much smaller.

Fig. 3. Hysteresis loop (solid line) and initial magnetization (dashed line) of a 60-nm LPCMO film is measured in the in-plane (*A*) and out-of-plane (*B*) direction, before and after the highest density antidots (D5) fabricated in it. Stronger magnetizations in antidot samples than in the film in both directions are shown. (*A* and *B*, *Insets*) Detailed information of the hysteresis loop around zero field.

better MFM imaging contrast because the easy magnetization axis is parallel to the surface. Even with a 2-T perpendicular field, there is enough perpendicular component of magnetization that allows us to view the FMM rings in MFM (Fig. S3), although with an understandably weaker imaging contrast. Based on the percentage of the antidot-induced enhancement of the saturation

magnetization and the volume ratio of the ferromagnetic rings, we estimate that the saturation magnetization of the ferromagnetic rings is about 16% higher than that of the film without antidots.

To explain the experimental observations, we establish a model and carry out numerical simulations. The FMM rings around the antidots serve as nuclei sites for the expansion of

Fig. 4. MFM images acquired during 5-T field cooling show four antidots in the second lowest density antidot sample (D2) at 200, 140, 80, and 20 K. The color scales are set as −45°, −24°, −20°, and −15°, respectively. The colored scales are set with the same zero point but not the same value because the signals at low temperature are much stronger than that at high temperature. The R–T curve is the corresponding cooling curve in Fig. 2*D*. Preference of ferromagnetic states around the antidots is shown in the MFM images at 200 and 140 K and the FMM rings become clear at 80 and 20 K. Around these FMM rings, these stronger magnetic signals slowly spread and decay to the values of the normal film.

Fig. 5. Monte Carlo simulation of the temperature dependence of normalized resistance for different density of antidot samples at (A) B = 0, (B) B = 0.2J, and (C) B = 0.67J. In the low-density model, the distance between adjacent antidots is 10× the antidot radius, whereas in the high-density one this ratio is 6. Simulation results are consistent with transport measurement data both in the MIT temperature and normalized resistance behavior.

FMM phase during the cooling process and assist the percolation process.

We divide the film into 350×350 pixels and define their magnetic states with a spin s. For simplicity, we use the Ising model and the Monte Carlo method for studies of the phase transition (23),

$$H = -J \sum_{\langle ij \rangle} s_i s_j + \sum_{[ik]} J'_{ik} s_i s_k - B \sum_i s_i, \qquad [1]$$

where s_i are the Ising variables, B is the external magnetic field, J is the nearest-neighbor ferromagnetic coupling, and J'_{ik} is the next-nearest-neighbor antiferromagnetic coupling. As known, LPCMO films tend to have stronger magnetization at the edge, which can be described by an enhanced J or reduced J' in those regions. In the present work, the edge ferromagnetism is incorporated by setting $J' = 0$ for pixels that are within three rows near the edge (16). In the interior region, J'_{ik} is calculated from a

random field, $J'_{ik} = J'(1 + \varepsilon_{ik})$, with ε_{ik} reflecting the effect of long-range correlation of the disorder in the following manner (23):

$$\varepsilon_{ik} = \sum_j \frac{h_{jk}}{\left(1 + d_{ij}^2\right)^{\alpha/2}}, \qquad [2]$$

where h_{jk} stands for the random fields at four next-nearest-neighbors k around the pixel j. The best agreement with experiment is found when $\alpha = 6$.

For transport studies, we define that a pixel belongs to a metallic domain if more than 70% of its neighboring pixels are aligned in the same direction at the end of Monte Carlo steps following the Metropolis algorithm, otherwise it belongs to the insulating domain. The conductivity of the metallic domain varies with temperature as $\sigma_M = \sigma_0/(1 + cT)$ while that of the insulating domain is $\sigma_I = \exp(-E_t/k_B T)$, with an assumption $E_t = 10J$. The total resistance of the network is solved from the current continuity equation, $\nabla \cdot \sigma \nabla \phi = 0$, where ϕ is the potential with the boundary condition supplied by the bias voltage. The current density across the pixels is calculated from $\sigma \nabla \phi$ and the total resistance can be obtained from the ratio between the bias voltage and current. Hysteresis is an important aspect of CMR R–T curves. However, unlike magnetic hysteresis curves of ferromagnetic materials, the R–T curves of CMR materials are strongly time dependent, which means that for infinitely slow measurements the hysteresis can be very small. To use the simplest possible model to explain our experiment, we will neglect hysteresis in our model, thus removing the need to assume an energy barrier for switching the spins.

The results of simulations for samples of high and low antidot densities are shown in Fig. 5 A and C for B = 0, 0.2J, and 0.67J, respectively (for simulated patterns see Fig. S4). The fluctuations reflect intrinsic noise in Monte Carlo simulation. For the low-density configuration, the distance between adjacent antidots is 10× the antidot radius, whereas for the high-density one this ratio is 6. For ease of comparison, the resistance is also normalized with respect to the value at 300 K. Obviously, our simulations capture the main essences of experimental observations, i.e., the higher MIT temperature and lower resistance for samples with antidot arrays and the convergence of transport behaviors of different samples in large magnetic field.

The MFM data indicate that antidots facilitate the growth of FMM phase around them due to the enhancements of magnetization and magnetic ordering around the edges of antidots. Simulations verify these FMM rings are the reasons for the higher MIT temperature. In turn, the expansion of the FMM phase offers more connecting channels for the percolation, which leads to lower resistance of samples with high-density antidots at zero and small fields. The convergence of the MIT temperatures and resistances at large fields is natural because the external magnetic field plays the major role for the population of ferromagnetic phase and the effect of FMM rings becomes minor (24, 25).

In summary, we designed and studied LPCMO films with antidots and found strongly enhanced MIT temperature and reduced resistance, particularly in samples with higher antidot density. Based on Monte Carlo simulations with a simple model Hamiltonian, we attributed the mechanism to the enhancement of magnetization and magnetic ordering around the edges of antidots in LPCMO films. This work offers a way to control the physical properties of CMR manganites without changing the doping concentration, introducing new materials, or applying external fields. Moreover, the successful creation of ordered arrays of FMM rings in manganites opens an avenue to electronically pattern complex oxides for better tunability of their performance in electronic and spintronic devices.

PHYSICS

1. Tokura Y (2006) Critical features of colossal magnetoresistive manganites. *Rep Prog Phys* 69(3):797–851.
2. Dagotto E, Hotta T, Moreo A (2001) Colossal magnetoresistant materials: The key role of phase separation. *Phys Rep* 344(1-3):1–153.
3. Moreo A, Yunoki S, Dagotto E (1999) Phase separation scenario for manganese oxides and related materials. *Science* 283(5410):2034–2040.
4. Dagotto E (2005) Complexity in strongly correlated electronic systems. *Science* 309(5732):257–262.
5. Liang L, Li L, Wu H, Zhu X (2014) Research progress on electronic phase separation in low-dimensional perovskite manganite nanostructures. *Nanoscale Res Lett* 9(1):325.
6. Salamon M, Jaime M (2001) The physics of manganites: Structure and transport. *Rev Mod Phys* 73(3):583–628.
7. Uehara M, Mori S, Chen CH, Cheong SW (1999) Percolative phase separation underlies colossal magnetoresistance in mixed-valent manganites. *Nature* 399(6736):560–563.
8. Zhang L, Israel C, Biswas A, Greene RL, de Lozanne A (2002) Direct observation of percolation in a manganite thin film. *Science* 298(5594):805–807.
9. Kim TH, et al. (2010) Imaging and manipulation of the competing electronic phases near the Mott metal-insulator transition. *Proc Natl Acad Sci USA* 107(12):5272–5275.
10. Ward TZ (2009) Elastically driven anisotropic percolation in electronic phase-separated manganites. *Nat Phys* 5:885–888.
11. Lai K, et al. (2010) Mesoscopic percolating resistance network in a strained manganite thin film. *Science* 329(5988):190–193.
12. Ward TZ, et al. (2011) Tuning the metal-insulator transition in manganite films through surface exchange coupling with magnetic nanodots. *Phys Rev Lett* 106(15):157207.
13. Guo H, et al. (2013) Electrophoretic-like gating used to control metal-insulator transitions in electronically phase separated manganite wires. *Nano Lett* 13(8):3749–3754.
14. Martin JI, Nogues J, Liu K, Vicent JL, Schuller IK (2003) Ordered magnetic nanostructures: Fabrication and properties. *J Magn Magn Mater* 256(1-3):449–501.
15. Li H, et al. (2014) Giant intrinsic tunnel magnetoresistance in manganite thin films etched with antidot arrays. *Appl Phys Lett* 104(8):082414.
16. Kovylina M, et al. (2009) Tuning exchange bias in Ni/FeF_2 heterostructures using antidot arrays. *Appl Phys Lett* 95(15):152507.
17. Du K, et al. (2015) Visualization of a ferromagnetic metallic edge state in manganite strips. *Nat Commun* 6:6179.
18. Ma JX, Gillaspie DT, Plummer EW, Shen J (2005) Visualization of localized holes in manganite thin films with atomic resolution. *Phys Rev Lett* 95(23):237210.
19. Ward TZ, et al. (2008) Reemergent metal-insulator transitions in manganites exposed with spatial confinement. *Phys Rev Lett* 100(24):247204.
20. Frankovsky R, et al. (2013) Short-range magnetic order and effective suppression of superconductivity by manganese doping in $LaFe_{1-x}Mn_xAsO_{1-y}F_y$. *Phys Rev B* 87(17):174515.
21. Urushibara A, et al. (1995) Insulator-metal transition and giant magnetoresistance in $La_{1-x}Sr_xMnO_3$. *Phys Rev B Condens Matter* 51(20):14103–14109.
22. Mahendiran R, et al. (2002) Ultrasharp magnetization steps in perovskite manganites. *Phys Rev Lett* 89(28 Pt 1):286602.
23. Burgy J, Moreo A, Dagotto E (2004) Relevance of cooperative lattice effects and stress fields in phase-separation theories for CMR manganites. *Phys Rev Lett* 92(9):097202.
24. Tomioka Y, Asamitsu A, Moritomo Y, Kuwahara H, Tokura Y (1995) Collapse of a charge-ordered state under a magnetic field in $Pr_{1/2}Sr_{1/2}MnO_3$. *Phys Rev Lett* 74(25):5108–5111.
25. Tokunaga M, Miura N, Tomioka Y, Tokura Y (1998) High-magnetic-field study of the phase transitions of $R_{1-x}Ca_xMnO_3$ (R=Pr, Nd). *Phys Rev B* 57(9):5259–5264.